Trajectory-Aware Cross-Paradigm Transformers for Efficient System Matrix Calibration in Magnetic Particle Imaging

Jintao Li[1,†], Lizhi Zhang[1,†], Xiaowei He[1], Shuaishuai He[1], Shuangchen Li[2], Bo Shi[3], Yuqing Hou[1], and Hongbo Guo[1,*]

[1] School of Information Sciences and Technology, Northwest University, Xi'an, 710127, China.
[2] Center for Biomedical Imaging Research, School of Biomedical Engineering, Tsinghua University, Beijing, 100084, China.
[3] Gina Cody School of Engineering and Computer Science, Concordia University, Montreal, Canada
[†] Co-first authors; * Corresponding author: guohb@nwu.edu.cn

Abstract. Magnetic particle imaging (MPI) is an emerging medical imaging modality that enables highly sensitive visualization of magnetic nanoparticles with high temporal resolution. However, variations in magnetic particle materials and field-free point trajectories require repeated system matrix recalibration, which is time-consuming and limits the efficiency and flexibility of MPI in practical applications. To address this challenge, we propose a trajectory-aware cross-paradigm transformer (TACPT) for efficient and accurate SM calibration. Leveraging the trajectory-dependent distribution of SM signals relative to FFPs, we introduce a trajectory-based encoding mechanism that embeds physically grounded positional priors derived from FFP trajectories into the transformer backbone. This design guides the network to focus on trajectory-relevant and information-dense regions. To further accommodate the complex structure of SM data, we develop a cross-paradigm feature interaction module that integrates FFT-based inter-channel modeling with spatial structure learning. These complementary representations are adaptively fused through a dynamic sparsity-gated mechanism, suppressing redundant responses and producing compact, discriminative SM representations. Experimental results demonstrate superior SM calibration and MPI reconstruction performance over existing methods, while reducing recalibration overhead without compromising fidelity to improve MPI system efficiency and flexibility. The code is publicly available at `https://github.com/learning-TL/TACPTnet`.

Keywords: Magnetic Particle Imaging · System Matrix Calibration · Trajectory-Aware Encoding · Cross-Paradigm Transformers.

1 Introduction

Magnetic Particle Imaging (MPI) is an emerging medical imaging modality that enables highly sensitive and quantitative visualization of superparamagnetic nanoparticles with high spatiotemporal resolution by directly detecting tracer-specific signals[27, 20]. Owing to these advantages, MPI has been extensively investigated in preclinical studies for applications such as angiography[5, 2], stem cell tracking[30, 17], cancer imaging[26, 25, 21], lung perfusion imaging[29], and localized magnetic hyperthermia treatment for cancer[4].

Magnetic particle imaging (MPI) reconstruction is commonly formulated using either X-space or system matrix (SM)-based approaches[22, 11]. While X-space methods model MPI as a linear and shift-invariant system with a well-behaved point spread function[9, 8], their neglect of practical system physics often leads to reconstruction artifacts and incomplete edge information. In contrast, SM-based methods formulate MPI as a constrained linear inverse problem and generally achieve higher reconstruction accuracy by explicitly incorporating system knowledge and regularization priors[1, 11]. However, accurate SM calibration requires exhaustive sampling of the imaging field of view on dense volumetric grids, resulting in substantially increased measurement time, particularly for large fields of view[16, 19, 10]. To alleviate this limitation, recent studies have demonstrated the feasibility of directly upscaling low-resolution volumetric grids to high-resolution SMs. Representative methods cover a wide range of super-resolution paradigms, including traditional interpolation techniques such as bicubic and cubic interpolation[12, 14], CNN-based approaches such as SRCNN[6] and 3d-SMRnet[3], PPGnet[7], hybrid convolution–transformer models such as TranSMS[10], MKD-SM[13], and progressive upscaling frameworks including 3dISPAnet[28], LapSRN[18], and ProTSM[24]. Despite these advances, the effectiveness of existing approaches remains constrained by the intrinsic characteristics of SM data. Unlike natural images, SM signals are highly concentrated near the field-free point (FFP) trajectory, yet most existing models lack explicit trajectory-aware feature prioritization, limiting their ability to distinguish information-rich regions from noise-dominated background areas under high undersampling ratios. Moreover, many architectures model spatial structures and channel dependencies in a largely decoupled manner, which is insufficient to capture the strong coupling between local spatial variations and global channel distributions inherent in compact SM response patterns.

In response to these issues, we propose a trajectory-aware cross-paradigm transformer (TACPT) for efficient system matrix calibration in magnetic particle imaging. Distinct from purely data-driven designs, TACPT-Net embeds the physical characteristics of SM signal formation into the transformer architecture by introducing a trajectory-aware encoding mechanism. Leveraging the trajectory-correlated distribution of SM signals with respect to the field-free point, this mechanism injects physically grounded positional priors into the transformer backbone, guiding the model to emphasize trajectory-related informative signal regions. Furthermore, TACPT incorporates a cross-paradigm feature interaction strategy that jointly captures FFT-based inter-channel dependencies and spatial structural information. These complementary features are then integrated through a dynamic sparsity-gated fusion mechanism, which preserves physically meaningful SM representations while mitigating redundancy

and noise, thereby improving reconstruction fidelity under reduced calibration measurements. The main contributions of this work are threefold:
(1) We propose a trajectory-aware cross-paradigm transformer (TACPT) for efficient MPI system matrix calibration, explicitly aligning transformer-based modeling with the physical characteristics of SM signal formation.
(2) We introduce a trajectory-aware encoding mechanism that embeds FFP-referenced positional priors into the transformer backbone to model trajectory-dependent SM signal distributions, thereby improving robustness and generalization across diverse scanning trajectories.
(3) We develop a cross-paradigm feature interaction strategy that integrates FFT-based inter-channel and spatial structural information via a dynamic sparsity gated fusion mechanism to preserve compact SM responses while reducing redundancy and noise.

2 Method

As illustrated in Fig. 1, TACPT-Net calibrates a high-resolution (HR) system matrix volume $\hat{S}_{HR}$ from a low-resolution (LR) input $\hat{S}_{LR}$ through a dual-branch architecture that combines trajectory-aware encoding with calibration-oriented feature modeling. In MPI system matrix (SM) calibration, non-uniform trajectory coverage and spatially varying receive sensitivity result in pronounced heterogeneity of SM quality across the imaging volume. Voxels that are effectively excited and repeatedly sampled by the field-free point (FFP) trajectory typically exhibit higher signal fidelity, whereas sparsely covered regions are more susceptible to noise contamination, especially under reduced calibration measurements. To exploit this trajectory-dependent physical prior, we introduce a trajectory-aware encoding branch (TAEB) that explicitly incorporates voxel-wise trajectory relevance into positional embeddings for physically informed feature modeling. In parallel, the calibration branch takes $\hat{S}_{LR}$ as input and extracts shallow representations using convolutional layers, followed by refinement through a stack of self-attention transformer layers (SATLs). Each SATL incorporates a Cross-Paradigm Feature Interaction Module (CP-FIM), which consists of channel-aware attention and spatial-aware attention submodules, coupled by a dynamic sparsity-gated fusion block to jointly model inter-channel dependencies and spatial structural information. Finally, a lightweight reconstruction head based on PixelShuffle upsampling maps the refined features to the reconstructed HR system matrix $\hat{S}_{HR}$. Next, we will introduce the main parts of our model as follows:

(1)Trajectory Aware Encoding Branch (TAEB): As illustrated in Fig. 1 (b), the proposed TAEB incorporates field-free point trajectory priors to construct trajectory-aware positional embeddings for the transformer backbone. Specifically, the FFP trajectory is defined by the drive-field signals $x(t) = A_x \sin(2\pi f_x t),\ y(t) = A_y \sin(2\pi f_y t),\ z(t) = A_z \sin(2\pi f_z t)$ from which the instantaneous FFP position $\mathbf{p}_{\text{FFP}}(t)$ is obtained via physical coordinate mapping. For each voxel with physical coordinates $\mathbf{p}_v^{(i)}$, TAEB evaluates its trajectory rel-

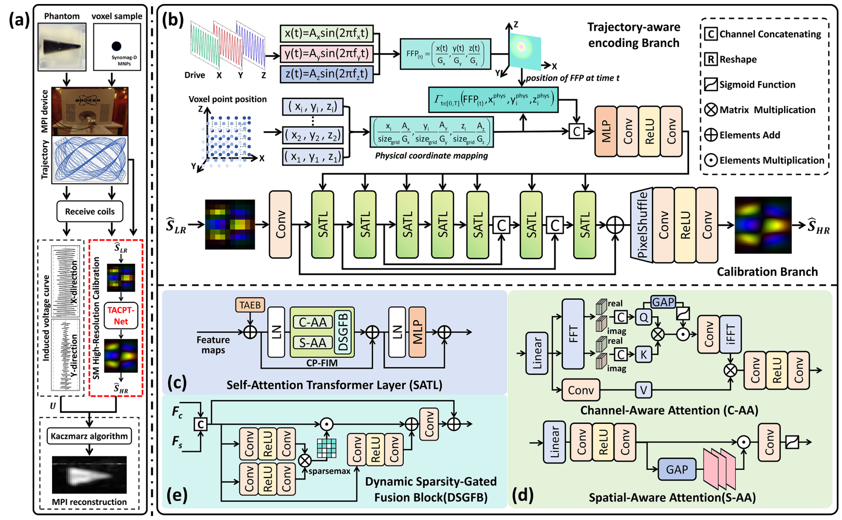

Fig. 1. (a) The MPI Reconstruction Process. (b) NTACPT-Net with calibration and trajectory-aware encoding branches. (c) Self-attention transformer layer (SATL) with TAEB-injected trajectory-aware positional embeddings. (d) Cross-paradigm feature interaction module (CP-FIM) with channel- and spatial-aware attention. (e) Dynamic sparsity-gated fusion block for adaptive fusion of channel and spatial features.

evance by measuring the minimum spatial distance to the field-free point (FFP) trajectory and assigning a position-wise importance weight:

$$\mathrm{match}(i) = \exp\left(-\frac{\lambda}{s^4} \min_{k\in\{1,\ldots,T\}} \left\|\mathbf{p}_{\mathrm{FFP}}(t_k) - \mathbf{p}_v^{(i)}\right\|_2^4\right), \tag{1}$$

where $\mathbf{p}_{\mathrm{FFP}}(t_k)$ denotes the discretely sampled FFP trajectory, T is the number of trajectory samples, s is the spatial normalization scale related to the drive-field amplitudes, and λ controls the decay rate. The fourth-order distance term prioritizes trajectory-related voxels in sparsely sampled regions. Next, the voxel coordinates $\mathbf{p}_v^{(i)}$ are concatenated with the trajectory-aware weight match(i) to form a physical positional descriptor, which is mapped to a trajectory-aware positional embedding via a lightweight MLP followed by convolution:

$$e_i = \mathrm{Conv}\Big(\mathrm{MLP}\Big([\mathbf{p}_v^{(i)}, \mathrm{match}(i)]\Big)\Big), \tag{2}$$

where e_i denotes the trajectory-aware positional embedding of the i-th voxel, which is injected into the transformer backbone to enable trajectory-guided feature modulation and trajectory-consistent attention learning.

(2) Self-Attention Transformer Layer (SATL): As shown in Fig. 1(c), the calibration branch employs stacked Self-Attention Transformer Layers as the primary building blocks for feature refinement. Given the input feature $X \in \mathbb{R}^{N\times C}$, TAEB provides trajectory-aware positional embeddings $E \in \mathbb{R}^{N\times C}$, which are injected into the transformer backbone. The SATL is formulated as:

$$Z = X + E, \quad X' = Z + \mathcal{F}_{CP}\big(\mathrm{LN}(Z)\big), \quad Y = X' + \mathrm{MLP}\big(\mathrm{LN}(X')\big) \tag{3}$$

where $\mathcal{F}_{CP}(\cdot)$ denotes the proposed Cross-Paradigm Feature Interaction Module (CP-FIM), and $\mathrm{LN}(\cdot)$ represents layer normalization. $\mathrm{MLP}(\cdot)$ denotes the position-wise feed-forward network consisting of two linear transformations with a non-linear activation. N is the number of voxel tokens, and C denotes the channel dimension of the transformer.

(3)Cross-Paradigm Feature Interaction Module (CP-FIM): The proposed CP-FIM serves as the core interaction module in each SATL, integrating channel-aware attention(C-AA) and spatial-aware attention(S-AA) with dynamic sparsity-gated fusion block (DSGFB). Within CP-FIM, the C-AA branch is designed to model long-range inter-channel dependencies in MPI system matrices. Given an input feature map, query, key, and value embeddings are first generated through linear projections. To exploit the inherent spectral structure of MPI signals, fast Fourier transform (FFT) is selectively applied to the query and key embeddings, enabling effective characterization of global channel correlations in the frequency domain. The resulting frequency-domain query–key correlations are further regulated through a query-guided global modulation mechanism, where a global channel descriptor obtained via global average pooling of the query embedding adaptively weights the correlation responses. Then apply the modulated attention weights to the spatial domain value embeddings for convolutional refinement to generate channel-aware outputs. In parallel, the S-AA branch computes spatial attention using standard convolutional and pooling operations to emphasize spatially informative regions. The structures of the C-AA and S-AA branches are illustrated in Fig. 1(d).

The outputs of the two branches are integrated within CP-FIM through the proposed Dynamic Sparsity-Gated Fusion Block (DSGFB), as shown in Fig. 1(e). The channel-aware and spatial-aware features are first concatenated along the channel dimension to form a unified fused representation. This representation is processed by parallel lightweight convolutional transformations to generate fusion weight responses that encode diverse channel-spatial interaction patterns. The DSGFB then estimates a data-dependent sparse gating map via the sparsemax operator, allowing the fusion pattern to adapt dynamically across samples and feature locations while suppressing redundant activations. In contrast to soft gating mechanisms that uniformly scale all feature components, the sparsemax-based gating enables explicit and structured sparsity, yielding a compact fusion representation that aligns with the inherently localized response characteristics of MPI system matrices. The sparsely gated feature is subsequently processed through a lightweight convolutional transformation, and the resulting representation is finally combined with a residual connection to preserve essential information and ensure stable optimization.

3 Experiments and Results

3.1 Data preparation and Implementation Details

Training data were acquired using Synomag-D MNPs (Micromod GmbH, Germany) with a 3D Lissajous FFP trajectory[16]. Signals with SNR ≥ 5 and frequency ≥ 70 kHz were segmented into 3D independent samples and zero-padded to an HR size of $40 \times 40 \times 40$. Corresponding LR volumes were generated by downsampling with factors of 2 and 4, yielding sizes of $20 \times 20 \times 20$ and $10 \times 10 \times 10$. In total, 2,736 samples were split into training (80%) and testing (20%) sets. Robustness to different MNP materials and FFP trajectories was further evaluated using two additional test datasets constructed under the same criteria[16]. Dataset details are summarized in Table 1.

All experiments were implemented in PyTorch 2.6 with Python 3.9 and conducted on an NVIDIA A6000 GPU. The network was trained for 200 epochs using the Adam optimizer with batch size of 128 and an initial learning rate of 1×10^{-4}. All convolutional layers use a kernel size of 3 and a stride of 1. For TAEB, the decay factor was fixed to $\lambda = 20$. The mean squared error (MSE) was used as the loss function. For image reconstruction based on calibrated SMs, the Kaczmarz algorithm[15] was applied with a step size of 1×10^{-1} for ten iterations.

Table 1. The details of the training and testing set based on the OpenMPI dataset.

Group	Calibrations	Particle	Trajectory	FOV(mm)	Samples
Training set	#7	Synomag-D	3D Lissajous	37×37×18.5	2189
Testing set	#7	Synomag-D	3D Lissajous	37×37×18.5	547
	#6	Perimag	3D Lissajous	37×37×18.5	1691
	#5	Perimag	2D Lissajous	37×37×18.5	139

3.2 Compared methods and Evaluation Metrics

Seven methods were compared, including two traditional interpolation baselines and five deep learning (DL)-based models. Bicubic[12] and Trilinear[14] interpolation were used as classical baselines. The DL-based methods include SRCNN[6], 3d-SMRnet[3], TranSMS[10], 3dISPAnet[28], and LapSRN[18], covering pre-upsampling CNNs, post-upsampling architectures, hybrid convolution transformer models, and progressive super-resolution strategies. Meanwhile, the normalized root-mean-square error (nRMSE), peak SNR (PSNR), and structure similarity index measure (SSIM) were selected to quantify the error between the recovered and the ground truth of HR, and also to verify the quality of the reconstructed MNPs distribution relative to the reference value[23, 24, 11].

3.3 Quantitative and Qualitative Results

SM Calibration and Reconstruction Evaluation: Fig. 2 compares the SM super-resolution results under 2× and 4× upsampling factors for different MNP materials and FFP trajectories, along with the corresponding Shape and Resolution phantom reconstructions under 4× upsampling, while Table 2 reports the quantitative evaluation of the phantom reconstructions. Interpolation-based methods suffer from severe blurring and loss of fine structures, while existing learning-based approaches still exhibit residual distortions, especially in trajectory-dependent regions. In contrast, the proposed method consistently produces more compact and structurally coherent SMs, leading to reconstructions with sharper boundaries, higher contrast, and improved separability of fine structures. Quantitatively, the proposed method consistently achieves the best performance across all configurations. Under 4× downsampling with Synomag-D and a 3D Lissajous trajectory, it attains an NRMSE of 0.0208 and an SSIM of 0.9021 on the Resolution phantom, corresponding to an average relative NRMSE reduction of over 10% and an SSIM improvement of approximately 1–2% compared with existing methods. Across six evaluation settings, it further achieves 6–17% NRMSE reduction over LapSRN, 0.3–0.6 dB PSNR improvement over 3dISPAnet, and 4–20% SSIM gains over interpolation-based methods.

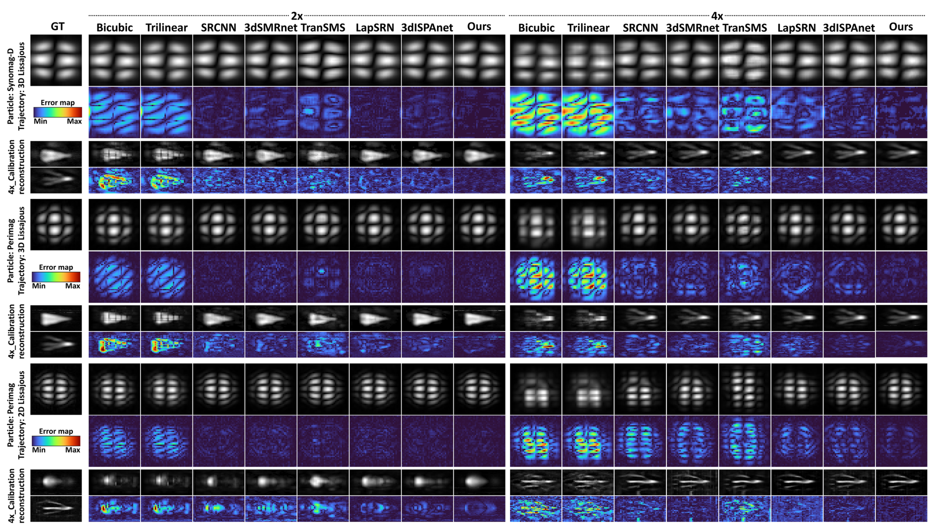

Fig. 2. Visualization of SM super-resolution results under 2× and 4× sampling for different tracer types and FFP trajectories, together with the corresponding Shape and Resolution phantom reconstructions under 4× sampling.

Ablation studies: Table 3 reports the quantitative ablation results for SM super-resolution under a 4× sampling ratio. Model_1 serves as the baseline, the

Table 2. Quantitative analysis results of the Shape and Resolution phantoms under $4\times$ sampling ratios in different imaging modes.

Mode	**Particle: Synomag-D Trajectory: 3D Lissajous**						**Particle: Perimag Trajectory: 3D Lissajous**						**Particle: Perimag Trajectory: 2D Lissajous**					
Phantoms	**Shape**			**Resolution**			**Shape**			**Resolution**			**Shape**			**Resolution**		
Metric	**nrmse**	**psnr**	**ssim**	**nrmse**	**psnr**	**ssim**	**nrmse**	**psnr**	**ssim**	**nrmse**	**psnr**	**ssim**	**nrmse**	**psnr**	**ssim**	**nrmse**	**psnr**	**ssim**
Bicubic	0.0857	25.31	0.5017	0.0883	28.41	0.5939	0.0893	25.02	0.4829	0.0921	27.98	0.5713	0.0879	25.13	0.4931	0.0907	28.19	0.5817
Trilinear	0.0779	26.07	0.5121	0.0806	28.82	0.6033	0.0811	25.84	0.4947	0.0837	28.36	0.5821	0.0797	25.97	0.5043	0.0821	28.63	0.5921
SRCNN	0.0314	31.78	0.7123	0.0336	35.61	0.8261	0.0367	30.92	0.6899	0.0388	35.02	0.8047	0.0327	31.21	0.6981	0.0348	35.28	0.8129
3dSMRnet	0.0278	32.11	0.7269	0.0299	36.46	0.8477	0.0331	31.26	0.7043	0.0352	36.01	0.8289	0.0289	31.67	0.7137	0.0311	36.23	0.8351
TranSMS	0.0497	29.12	0.6737	0.0521	35.07	0.8079	0.0549	28.41	0.6517	0.0573	34.63	0.7841	0.0519	28.76	0.6613	0.0542	34.91	0.7937
LapSRN	0.0239	32.63	0.7431	0.0261	37.08	0.8649	0.0287	31.79	0.7211	0.0309	36.47	0.8461	0.0247	32.16	0.7293	0.0269	36.71	0.8527
3dISPAnet	0.0216	33.14	0.7617	0.0238	38.33	0.8897	0.0262	32.33	0.7397	0.0284	37.86	0.8759	0.0223	32.71	0.7471	0.0246	38.02	0.8823
Ours	**0.0187**	**33.71**	**0.7789**	**0.0208**	**38.92**	**0.9021**	**0.0229**	**32.92**	**0.7561**	**0.0251**	**38.37**	**0.8893**	**0.0191**	**33.29**	**0.7639**	**0.0212**	**38.61**	**0.8951**

purely data-driven Transformer architecture is difficult to recover high-fidelity SM representations without incorporating domain-specific priors. Model_2 and Model_3 introduce TAEB and CP-FIM respectively, and both yield substantial performance improvements over the baseline, with PSNR increased by more than 1 dB compared to the baseline, demonstrating that TAEB and CP-FIM provide complementary and non-redundant gains. Starting from Model_3, the incorporation of channel-aware attention (Model_4) or spatial-aware attention (Model_5) further enhances reconstruction quality. Model_6 concatenates the C-AA and S-AA features without DSGFB, delivering additional gains but still underperforming the full model. The full model (Model_7), which integrates all proposed components, achieves the best performance across all metrics, reaching a PSNR of 34.60 dB and an SSIM of 0.941.

Table 3. Quantitative indicators for ablation studies at $4\times$ super resolution.

Group	**TAEB**	**CP-FIM**	**C-AA**	**S-AA**	**DSGFB**	**nrmse(4x)**	**psnr(4x)**	**ssim(4x)**	**Params**
model_1	×	×	×	×	×	0.0318	31.92	0.901	0.92 M
model_2	√	×	×	×	×	0.0251	33.62	0.921	0.99 M
model_3	×	√	√	√	√	0.0271	33.08	0.914	1.08 M
model_4	√	√	√	×	×	0.0226	33.71	0.924	1.13 M
model_5	√	√	×	√	×	0.0219	33.78	0.927	1.11 M
model_6	√	√	√	√	×	0.0211	34.05	0.932	1.17 M
model_7	√	√	√	√	√	0.0202	34.60	0.941	1.21 M

4 Conclusion

TACPT-Net presents a physics-informed and structure-aware framework for system matrix calibration in magnetic particle imaging. By explicitly incorporating trajectory-dependent priors and unifying complementary spectral and spatial modeling paradigms, the proposed design aligns data-driven learning with the intrinsic physical and structural characteristics of SM signals. This design facilitates compact and robust representation learning for acquisition scenarios with variable trajectories and delivers valuable complementary improvements to existing physics-guided calibration methods. Extensive experiments demonstrate superior SM recovery and MPI reconstruction performance over existing methods, while ablation analyses verify the complementary roles of trajectory-aware and cross-paradigm modeling in achieving stable and physically consistent calibration. Moreover, in terms of efficiency, TACPT-Net outperforms 3dISPAnet with fewer parameters (1.21M vs. 1.48M), lower FLOPs (1.25G vs. 1.55G), and faster inference (0.11s vs. 0.14s). In summary, by markedly reducing repeated SM recalibration overhead without sacrificing reconstruction fidelity, TACPT-Net enhances the efficiency and operational flexibility of MPI systems, providing a practical pathway toward scalable and adaptable MPI deployment. Future work will extend the evaluation to in vivo MPI and more SOTA baselines to further validate generalizability and clinical applicability.

Acknowledgments. This study was funded by the National Natural Science Foundation of China under Grants 12271434, 62271394, 62201459; The Scientific and Technological projects of Xi'an under Grant 201805060ZD11CG44; The Scientific and Technology New Star in Shaanxi Province of China under Grant 2023KJXX-035; General Project of the Key Research and Development Plan of Shaanxi Province under Grant 2025SF-YBXM-240; Natural Science Basic Research Plan in Shaanxi Province of China under Grant 2023-JC-JQ-57; Artificial intelligence empowers the team of "scientists + engineers" in education under 2024JH-KGDW-0084.

Disclosure of Interests. The authors have no conflicts to disclose.

References

1. Askin, B., Güngör, A., Alptekin Soydan, D., Saritas, E.U., Top, C.B., Cukur, T.: Pp-mpi: A deep plug-and-play prior for magnetic particle imaging reconstruction. In: International Workshop on Machine Learning for Medical Image Reconstruction. pp. 105–114. Springer (2022)
2. Bakenecker, A.C., Ahlborg, M., Debbeler, C., Kaethner, C., Buzug, T.M., Lüdtke-Buzug, K.: Magnetic particle imaging in vascular medicine. Innovative surgical sciences **3**(3), 179–192 (2018)
3. Baltruschat, I.M., Szwargulski, P., Griese, F., Grosser, M., Werner, R., Knopp, T.: 3d-smrnet: Achieving a new quality of mpi system matrix recovery by deep learning. In: Medical Image Computing and Computer Assisted Intervention–MICCAI 2020: 23rd International Conference, Lima, Peru, October 4–8, 2020, Proceedings, Part II 23. pp. 74–82. Springer (2020)
4. Chandrasekharan, P., Tay, Z.W., Hensley, D., Zhou, X.Y., Fung, B.K., Colson, C., Lu, Y., Fellows, B.D., Huynh, Q., Saayujya, C., et al.: Using magnetic particle imaging systems to localize and guide magnetic hyperthermia treatment: tracers, hardware, and future medical applications. Theranostics **10**(7), 2965 (2020)
5. Dietrich, P., Vogel, P., Kampf, T., Rückert, M.A., Behr, V.C., Bley, T.A., Herz, S.: Near real-time magnetic particle imaging for visual assessment of vascular stenosis in a phantom model. Physica Medica **81**, 210–214 (2021)

6. Dong, C., Loy, C.C., He, K., Tang, X.: Image super-resolution using deep convolutional networks. IEEE transactions on pattern analysis and machine intelligence **38**(2), 295–307 (2015)
7. Geng, X., Su, L., Bian, Z., Sun, Z., Wen, J., Tian, J., Du, Y.: Position-prior-guided network for system matrix super-resolution in magnetic particle imaging. In: 2025 47th Annual International Conference of the IEEE Engineering in Medicine and Biology Society (EMBC). pp. 1–7. IEEE (2025)
8. Goodwill, P.W., Conolly, S.M.: The x-space formulation of the magnetic particle imaging process: 1-d signal, resolution, bandwidth, snr, sar, and magnetostimulation. IEEE transactions on medical imaging **29**(11), 1851–1859 (2010)
9. Goodwill, P.W., Conolly, S.M.: Multidimensional x-space magnetic particle imaging. IEEE transactions on medical imaging **30**(9), 1581–1590 (2011)
10. Güngör, A., Askin, B., Soydan, D.A., Saritas, E.U., Top, C.B., Çukur, T.: Transms: Transformers for super-resolution calibration in magnetic particle imaging. IEEE Transactions on Medical Imaging **41**(12), 3562–3574 (2022)
11. Güngör, A., Askin, B., Soydan, D.A., Top, C.B., Saritas, E.U., Çukur, T.: Deq-mpi: A deep equilibrium reconstruction with learned consistency for magnetic particle imaging. IEEE Transactions on Medical Imaging (2023)
12. Gungor, A., Top, C.B.: Super-resolving reconstruction technique for mpi. International Journal on Magnetic Particle Imaging IJMPI **6**(2 Suppl 1) (2020)
13. Guo, P., Wei, Z., Zeng, Y., Wang, B., Liao, Y., Hu, J., Hou, L., Liu, K., He, N., Wang, Q., et al.: Multi-slice knowledge-driven system matrix calibration in magnetic particle imaging. IEEE Transactions on Computational Imaging **12**, 25–36 (2025)
14. Kasson, J.M., Nin, S.I., Plouffe, W., Hafner, J.L.: Performing color space conversions with three-dimensional linear interpolation. Journal of Electronic Imaging **4**(3), 226–250 (1995)
15. Knopp, T., Rahmer, J., Sattel, T.F., Biederer, S., Weizenecker, J., Gleich, B., Borgert, J., Buzug, T.M.: Weighted iterative reconstruction for magnetic particle imaging. Physics in medicine & biology **55**(6), 1577 (2010)
16. Knopp, T., Szwargulski, P., Griese, F., Gräser, M.: Openmpidata: An initiative for freely accessible magnetic particle imaging data. Data in brief **28**, 104971 (2020)
17. Kuo, R., Chandrasekharan, P., Fung, B., Conolly, S.: In vivo therapeutic cell tracking using magnetic particle imaging. International Journal on Magnetic Particle Imaging IJMPI **8**(1 Suppl 1) (2022)
18. Lai, W.S., Huang, J.B., Ahuja, N., Yang, M.H.: Deep laplacian pyramid networks for fast and accurate super-resolution. In: Proceedings of the IEEE conference on computer vision and pattern recognition. pp. 624–632 (2017)
19. Li, S., Zhang, L., Guo, H., Li, J., Yu, J., He, X., Zhao, Y., He, X.: Csa-fcn: Channel- and spatial-gated attention mechanism based fully complex-valued neural network for system matrix calibration in magnetic particle imaging. IEEE Transactions on Computational Imaging (2025)
20. Panagiotopoulos, N., Duschka, R.L., Ahlborg, M., Bringout, G., Debbeler, C., Graeser, M., Kaethner, C., Lüdtke-Buzug, K., Medimagh, H., Stelzner, J., et al.: Magnetic particle imaging: current developments and future directions. International journal of nanomedicine pp. 3097–3114 (2015)
21. Parkins, K.M., Melo, K.P., Chen, Y., Ronald, J.A., Foster, P.J.: Visualizing tumour self-homing with magnetic particle imaging. Nanoscale **13**(12), 6016–6023 (2021)
22. Shang, Y., Liu, J., Liu, Y., Wang, Y., Shen, Y., Wu, X., Zhang, L., Hui, H., Tian, J.: Spatial-frequency multi-scale transformer for deblurring and shape-preserving

reconstruction in magnetic particle imaging. IEEE Transactions on Computational Imaging (2024)
23. Shang, Y., Liu, J., Zhang, L., Wu, X., Zhang, P., Yin, L., Hui, H., Tian, J.: Deep learning for improving the spatial resolution of magnetic particle imaging. Physics in Medicine & Biology **67**(12), 125012 (2022)
24. Shi, G., Yin, L., An, Y., Li, G., Zhang, L., Bian, Z., Chen, Z., Zhang, H., Hui, H., Tian, J.: Progressive pretraining network for 3d system matrix calibration in magnetic particle imaging. IEEE Transactions on Medical Imaging (2023)
25. Tomitaka, A., Arami, H., Gandhi, S., Krishnan, K.M.: Lactoferrin conjugated iron oxide nanoparticles for targeting brain glioma cells in magnetic particle imaging. Nanoscale **7**(40), 16890–16898 (2015)
26. Yu, E.Y., Bishop, M., Zheng, B., Ferguson, R.M., Khandhar, A.P., Kemp, S.J., Krishnan, K.M., Goodwill, P.W., Conolly, S.M.: Magnetic particle imaging: a novel in vivo imaging platform for cancer detection. Nano letters **17**(3), 1648–1654 (2017)
27. Zhang, L., Li, J., Du, J., Fang, G., Zhang, D., Tang, Z., Guo, H., He, X.: Current reconstruction approaches of magnetic particle imaging: A review. Journal of Magnetism and Magnetic Materials p. 171894 (2024)
28. Zhang, L., Li, J., He, X., Tang, Z., Li, S., Zhao, Y., Guo, H.: Iterative up-and-down sampling network based on pyramid pooling and attention mechanism for 3d system matrix recovery in mpi. IEEE Transactions on Instrumentation and Measurement (2025)
29. Zhou, X.Y., Jeffris, K.E., Elaine, Y.Y., Zheng, B., Goodwill, P.W., Nahid, P., Conolly, S.M.: First in vivo magnetic particle imaging of lung perfusion in rats. Physics in Medicine & Biology **62**(9), 3510 (2017)
30. Zhou, X.Y., Tay, Z.W., Chandrasekharan, P., Yu, E.Y., Hensley, D.W., Orendorff, R., Jeffris, K.E., Mai, D., Zheng, B., Goodwill, P.W., et al.: Magnetic particle imaging for radiation-free, sensitive and high-contrast vascular imaging and cell tracking. Current opinion in chemical biology **45**, 131–138 (2018)